Hyperspectral drone images indicate that green shoulder indices are robust in pre-emergence detection of spruce bark beetle infestation across spatial and temporal scales

Luiz Henrique Elias Cosimo¹, Eva Lindberg¹, Henrik Persson¹, Jonas Bohlin¹, Langning Huo¹

¹Department of Forest Resource Management, Swedish University of Agricultural Sciences, S-901 83 Umeå, Sweden – {luiz.cosimo, eva.lindberg, henrik.persson, jonas.bohlin, langning.huo}@slu.se

Keywords: European spruce bark beetle, *Ips typographus*, forest damage, forest disturbance.

Abstract

Bark beetle (*Ips typographus* L.) outbreaks are one of the main threats to forest health in northern Europe, with recent events causing extensive damage to spruce forests. While management for population control relies on detecting infested trees before the emergence of the filial generation, identifying robust spectral indicators remains a major challenge. In this study, we evaluate the performance of vegetation indices (VIs) derived from hyperspectral drone imagery for detecting bark beetle infestations in southern Sweden. We calculated detection rates based on the cases where VI values for infested trees deviated from the value range observed in healthy trees. We tested different scenarios for defining the range of healthy values to assess spatial and temporal consistency of VI performance. Green shoulder VIs, particularly GSCR1_{MS} and GSCR2_{MS}, consistently showed the highest detection rates. Their performance was stable across different weeks and forest stands, indicating stronger generalizability and higher potential for pre-emergence detection. In contrast, red edge VIs showed limited temporal consistency and strong dependence on normalization. SWIR-based VIs presented low detection rates in all scenarios, therefore showing limited potential.

1. Introduction

The European spruce bark beetle (*Ips typographus* L.) has caused extensive damage in Swedish forests, threatening forest health, timber production, and socio-ecological values (Kärvemo et al., 2023). Developing effective remote sensing methods to detect infested trees as early as possible can support outbreak monitoring and response strategies (Luo et al., 2023).

Recent research has focused on pre-emergence detection to enable timely interventions and prevent further spread to healthy stands (Kautz et al., 2024). In other words, previous studies have investigated the possibility of identifying infested trees before offspring emergence, which typically occurs in Sweden around 9-10 weeks after bark beetle colonization depending on weather conditions (Öhrn et al., 2014). However, a key challenge remains in identifying reliable remote sensing indicators that can detect early stress signals across varying environmental and forest conditions.

The first study in Sweden to explore pre-emergence detection using multispectral drone imagery introduced novel vegetation indices (VIs) based on the red-edge region (680-780 nm), achieving detection rates of 15 and 90% of infested trees after 5 and 10 weeks of infestation, respectively (Huo et al., 2023a). A follow-up study demonstrated that machine-learning models trained on these VIs performed poorly when applied to untrained areas, highlighting challenges in generalizability (Huo et al., 2023b).

More recently, a study conducted in Finland proposed novel VIs based on the green shoulder region (490-560 nm), which provided the highest detection rates of bark beetle-infested trees among the tested VIs (Huo et al., 2024). That study also suggested that normalizing VI values using the first image acquired in a time series could further enhance detection rates. However, the transferability and robustness of these methods across regions remains untested.

In this study, we assess the performance of traditional and newly developed VIs to detect bark beetle infestation in southern Sweden using multi-temporal, high-resolution hyperspectral drone imagery. We focus particularly on evaluating VI robustness across different spatial and temporal scales to identify consistent and generalizable indicators for early stress detection.

2. Material and methods

The study was conducted in Remningstorp, Sweden (58°27′18″N, 13°39′8″E). The area is mainly composed of evenaged managed forest, where Norway Spruce and Scots Pine are the main occurring species. In 2023, we monitored four spruce forest stands, each containing six plots with a 15-meter radius, which included 30-60 trees.

A pheromone bag was placed in the central tree of each plot to attract bark beetles. Limitations from weather conditions led to poor bark beetle colonization in 17 out of the 24 field plots despite using pheromone bags, leading to unsuitable sites to represent outbreak scenarios. Therefore, the analysis focus on the 7 plots which experienced severe attacks, containing at least 5 infested trees (Table 1).

Stand and plot	Healthy	Infested	Total
st.1 - plt.6	39 (38)	5 (5)	44 (43)
st.2 - plt.3	41 (37)	5 (5)	46 (42)
st.2 - plt.5	53 (45)	7 (7)	60 (52)
st.3 - plt.1	32 (30)	10 (10)	42 (40)
st.3 - plt.4	33 (31)	5 (5)	38 (36)
st.3 - plt.6	24 (24)	11 (11)	35 (35)
st.4 - plt.6	22 (22)	14 (13)	36 (35)
Total	244 (227)	57 (56)	301 (283)

Table 1. Number of trees monitored in each plot. In parenthesis, the number of trees that were successfully segmented in the hyperspectral images using an automatic algorithm.

Weekly field inventories were conducted between weeks 16 and 32 to identify infested trees. According to symptom monitoring and bark beetle population monitoring, the swarming and attacks

by the overwintering generation occurred in weeks 19 and 20, the attacks by the sister generation occurred in week 23, and the F1 filial generation had peak emergence in weeks 28, 30, and 32.

Hyperspectral images were collected with cameras SPECIM AFX10 VNIR (400-1,000 nm, 224 bands, 7 cm GSD) and AFX17 SWIR (900-1,700 nm, 112 bands, 11 cm GSD), mounted one camera at a time on a multirotor drone Freefly Alta X with a Gremsy gimbal. The sensors were flown at 100 m height, resulting in 69 m swath. In each stand, we collected several parallel flight lines covering the field plot, spaced by 20 m.

VNIR and SWIR images were intended to be collected every second week from week 22 to week 32 of the year. However, in practice, image acquisition was limited by gimbal performance and logistics. In total, we conducted seven drone missions per camera. The first three flights occurred in different weeks for VNIR and SWIR. During the final four instances of image acquisition (weeks 26, 28, 30, and 32), images from both sensors were collected (Table 2).

Dataset	Week of 2023									
	16	18	20	22	23	24	26	28	30	32
Field	✓	✓	✓	✓	✓	✓	√	✓	✓	✓
AFX10	\checkmark_1	\checkmark_2			\checkmark_3		\checkmark	\checkmark	\checkmark	\checkmark
AFX17			\checkmark_1	\checkmark_2		$\sqrt{3}$	\checkmark	\checkmark	✓	\checkmark

Table 2. Timeframe of data collection. Datasets present for a given week are marked with the symbol ✓. Subscripted numbers represent normalization weeks tested for each camera.

Radiometric correction and georectification were performed using CaliGeoPRO software, resulting in imagery expressed in radiance units. The calibration coefficients for the camera pixels were derived under controlled laboratory conditions using a calibrated integrating sphere as a uniform radiance source. As specified by the manufacturer, 100 images of the sphere were averaged to generate a calibration image, and 100 dark frames were similarly averaged to correct for sensor noise. During each flight, ground reference targets with near-Lambertian surface were placed in the scene, and their known reflectance values were used to convert radiance to reflectance.

Treetops were identified in the images using single-band local maxima detection (550nm/AFX10, 965nm/AFX17) and tree crowns were segmented using a marker-controlled watershed segmentation. We then matched these treetops with the corresponding field observation using an automatic algorithm. Each field observation was first matched with all treetops within a 2.5 m radius, and the pair with the shortest distance was selected. Because cameras were flown with high side overlap, many trees were repeated in multiple flight lines, resulting in multiple segments in the same week. In such cases, we selected the crown segment closer to the central axis of the image to avoid off-nadir distortions. We also removed poor-quality crown segments (e.g., inaccurate treetop position, incorrect matching) based on spectral and visual assessments.

For each tree crown segment, pixels were selected among the 75% brightest pixels within 1-meter buffer around the treetop, which have previously been shown to be effective crown pixels (Huo et al., 2025). These pixels were extracted using a mask that was computed from the same bands used for segmentation for each camera (550nm/AFX10, 965nm/AFX17). The mask was created by removing reflectance values below the 25th percentile in those bands. Figure 1 illustrates crown segments (including the treetop and the 1-meter buffer from where spectral data was

extracted) for one of the field plots in the beginning and in the end of the study.

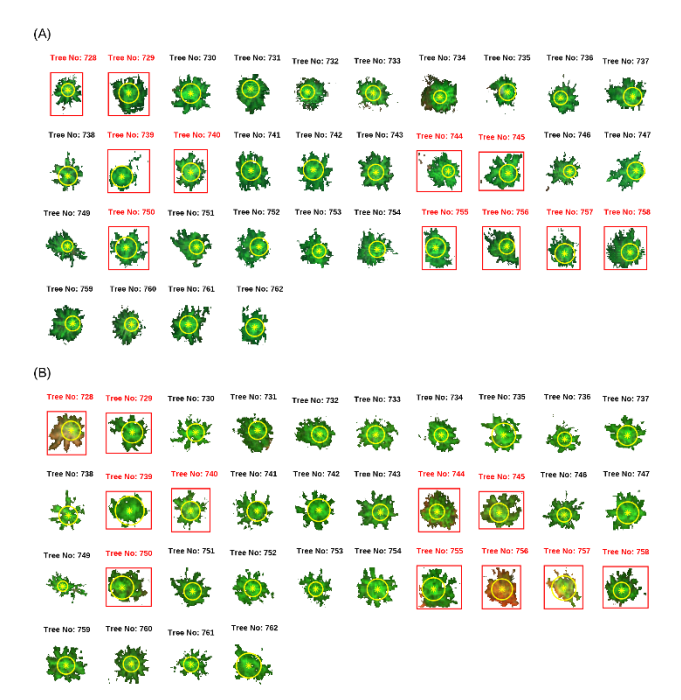


Figure 1. Tree crown segments from st.3-plt.6 in week 16 (A) and week 32 (B). Tree numbers are unique identifiers used in the study. Infested trees are highlighted with red squares around the crown segments. Tree tops are marked with yellow points, and 1-meter buffers are shown as yellow circles. Segments are true-colour composites based on AFX10-VNIR images using bands centred at 675 nm (red), 554 nm (green), and 479 nm (blue).

To make spectral signatures comparable across different flights, we used the Frobenius norm, defined as the square root of the sum of squares of reflectance values in the full spectra. We then smoothed the curves to minimize spectral noise using a spline function with a moderate smoothing factor (Green & Silverman, 1993) (Figure 2).

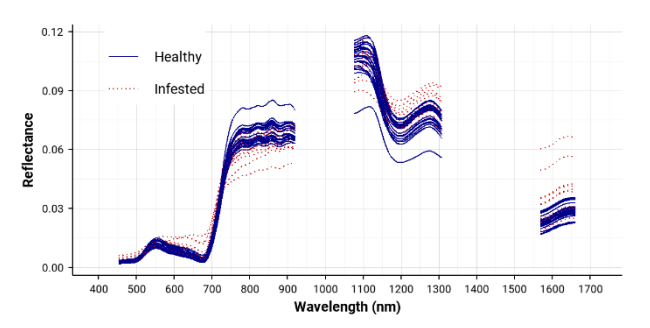


Figure 2. Reflectance curves (normalized and smoothed) for healthy and infested trees from st.4-plt.6 in week 32.

We calculated the first- and second-order derivatives based on the smoothed reflectance curves (Equations 1 and 2). Lastly, we calculated a series of VIs derived from reflectance values and spectral derivatives (Table 3).

$$R' = \frac{dR}{dW} = \frac{R_{i+1} - R_i}{W_{i+1} - W_i}$$
 (1)

$$R'' = \frac{d^2R}{d^2W} = \frac{d}{dW} \left(\frac{dR}{dW}\right) \tag{2}$$

where R = Reflectance
R' = first derivative
R'' = second derivative
W = wavelength
i = band index

Index	Definition	Reference
$GSIP_{520}$	Value of the maximum 1st	Huo et al.
	derivative at approx. 520 nm	(2024)
	T1	(-)
GSIP ₅₄₅	Value of the maximum 1st	Huo et al.
	derivative at approx. 545 nm	(2024)
GSCP ₅₃₀	Value of the maximum 2 nd	Huo et al.
GSC1 530		
	derivative at approx. 530 nm	(2024)
GSCR1	GSIP ₅₄₅	Huo et al.
	-GSCP ₅₃₀	(2024)
	330	
GSCR2	GSIP	Huo et al.
USCK2	$\frac{\text{GSIP}_{545}}{\text{GSIP}_{520} * -\text{GSCP}_{530}}$	
	$GSIP_{520} * -GSCP_{530}$	(2024)
REIP ₇₀₅ (a)	Value of the maximum 1st	Li et al.
	derivative at approx. 705 nm	(2024)
RECP ₆₈₅	Value of the maximum 2 nd	This study (b)
	derivative at approx. 685 nm	
DECD	Value of the minimum 2 nd	This study (b)
RECP ₇₀₅		This study (b)
	derivative at approx. 705 nm	
$GSCR1_{MS}$	$R_{550} - R_{530}$	Huo et al.
	$R_{530} - \left(\frac{R_{550} + R_{490}}{2}\right)$	(2024)
	$R_{530} - \left(\frac{330 + 330}{2}\right)$	
$GSCR2_{MS}$	$\frac{R_{550} - R_{530}}{(R_{530} - R_{490}) *}$	Huo et al.
OD CITEINS	(D D) :	(2024)
	$(R_{530} - R_{490}) *$	(2024)
	$\left(R_{530} - \frac{R_{550} + R_{490}}{2}\right)$	
PRI _{530/570}	$R_{531} - R_{570}$	Peñuelas et al.
	$R_{531} + R_{570}$	(1994)
PRI _{550/530}	$R_{550}^{331} - R_{530}^{370}$	Peñuelas et al.
1 1(1)30/330		(1994)
	$R_{550} + R_{530}$	
ARI	1 1	Gitelson et al.
	R ₅₅₀ R ₇₀₀	(2001)
CIG	$\frac{R_{865}}{R_{865}} - 1$	Gitelson et al.
	$\frac{803}{100} - 1$	(2003)
GT 17	R ₅₅₀	
CVI	$R_{865} * R_{705}$	Vincini et al.
	$R_{550} * R_{550}$	(2008)
GNDVI	$R_{780}^{550} - R_{550}^{550}$	Gitelson et al.
		(1996)
MD DOM	$R_{780} + R_{550}$	
$MR-DSWI_1$	$R_{705} * R_{705}$	Huo et al.
	$R_{550} * R_{783}$	(2023a)
$MR-DSWI_2$	$R_{705} * R_{705} * R_{865}$	Huo et al.
	D # D # D	(2023a)
MD DOM	$R_{550} * R_{783} * R_{783}$	` /
$MR-DSWI_3$	$R_{705} * R_{705} * R_{665}$	Huo et al.
	$R_{550} * R_{783} * R_{550}$	(2023a)
$MR-DSWI_4$	R ₇₀₅ * R ₇₀₅ * R ₈₆₅ * R ₆₆₅	Huo et al.
•	$R_{550} * R_{783} * R_{783} * R_{550}$	(2023a)
NDDE		
NDRE	$\frac{R_{790}-R_{720}}{R_{720}}$	Barnes et al.
	$R_{790} + R_{720}$	(2000)
NDVI	$R_{865} - R_{550}$	Rouse et al.
	$R_{865} + R_{550}$	(1973)
NGRDI	$R_{550} - R_{665}$	Tucker
NGKDI		
	$R_{550} + R_{665}$	(1979)
$REIP_{LI}$	700 + 40	Guyot et al.
	$(R_{670} - R_{780} - R_{780})$	(1988)
	$ * \left(\frac{\frac{R_{670} - R_{780}}{2} - R_{700}}{R_{740} - R_{700}} \right) $ $R_{718} - R_{748}$	/
	* \ \ \ \ \ \ \ \ \ \ \ \ \ \ \ \ \ \ \	
	\ \ \ \ \ \ \ \ \ \ \ \ \ \ \ \ \ \ \ \	
RVSI	R ₇₁₈ - R ₇₄₈ _	Merton
	$\frac{1}{2}$ - R ₇₃₃	(1998)
DRS		Huo et al.
מאס	$\left R_{ccr}^{2}+R_{ccr}^{2}\right $	
	$\frac{R_{718} - R_{748}}{2} - R_{733}$ $\sqrt{R_{665}^2 + R_{1610}^2}$	(2021)
NDII	$\frac{R_{819} - R_{1649}}{R_{819} + R_{1649}}$	Hardisky et al.
	$R_{910} + R_{1640}$	(1983)
	017 1047	

Index	Definition	Reference
NDWI	$R_{857} - R_{1241}$	Jackson et al.
	$R_{857} + R_{1241}$	(2004)
MSI	R ₁₆₀₀	Hunt & Rock
	R ₈₂₀	(1989)
RATIO ₉₇₅	$2*\overline{R}_{960-990}$	Pu et al.
	$\overline{R}_{920-940} + \overline{R}_{1090-110}$	(2004)
RATIO ₁₂₀₀	$2*\overline{R}_{1180-1220}$	Pu et al.
	$\overline{\overline{R}_{1090-1110} + \overline{R}_{1265-1285}}$	(2004)

Table 3. List of vegetation indices used in this study, as well as their definitions and sources. ^(a) referred to as REIP_d in Li at al. (2024), ^(b) derived from peaks and valleys observed in the second derivative curves in our data, inspired by REIP_d in Li at al. (2024) and GSCP₅₃₀ in Huo et al. (2024).

To determine whether a VI was capable of identifying infested trees, we first calculated a "healthy range", defined as the range of VI values presented by healthy trees (i.e., trees not infested with bark beetles). To minimize the influence of noise and outliers, we only considered VI values between the 1st and 99th percentiles. We assumed that this range encompassed the natural variability of trees in healthy conditions, and that a good VI would produce values deviating from the healthy range when trees are stressed.

For each VI and in each week, we labelled as detected any infested trees that presented values falling outside the healthy range. To assess spatial and temporal consistency, we considered three different scenarios for defining the healthy range:

- a. Individual-plot scenario a healthy range was defined individually for each field plot in each week of the study. Therefore, the detection of infested trees in this scenario only considered the healthy trees occurring in the same plot. This represented the finest scale of assessment, reflecting local site conditions.
- b. *Multi-stand scenario* a healthy range was defined for each week of the study, therefore considering simultaneously all healthy trees in a given week. This approach tests spatial consistency by pooling together the values observed for the healthy trees from all four stands in a given week.
- c. Multi-week scenario a single healthy range was defined for the entire study, therefore considering values observed for healthy trees in multiple weeks. We chose to restrict VI values obtained in weeks 26 and 32 to avoid fluctuations caused primarily by phenological changes occurring in spring (e.g. bud flush). This represented the broader scale of analysis, where detection depends on temporal consistency.

Furthermore, we tested if normalizing VIs considering the values obtained in early-season conditions could improve detection rates. We used a relative change normalization approach, which quantifies how much a VI has increased or decreased in relation to a baseline week (Equation 3). We tested normalization to the first three flights (denoted as norm-1, norm-2, or norm-3, in correspondence to Table 2) and we use the term "original values" to refer to VI values directly obtained from their formulas, i.e., without any normalization applied. For VIs based on AFX10 wavelengths (which was the case for most VIs in this study), baseline weeks corresponded to weeks 16, 18, or 23. For RATIO₁₂₀₀, which was based on AFX17 wavelengths, baseline weeks corresponded to weeks 20, 22, and 24. For other indices

based on wavelengths from both AFX10 and AFX17, we only analysed the original VI values due to the mismatch of baseline weeks for both cameras.

$$\delta VI = \frac{VI_i - VI_{baseline}}{VI_{baseline}}$$
 (3)

where $\delta VI = Normalized vegetation index$

VI = Vegetation index

i = week

baseline = week used for normalization

Finally, we calculated the detection rates at each week to compare the performance across VIs, healthy range scenarios (individual-plot, multi-stand, or multi-week), and normalization weeks (original values, norm-1, norm-2, or norm-3). The detection rate refers to the number of infested trees detected by a VI divided by the total number of infested trees (n = 56).

3. Results

In week 26, two weeks before the offspring emergence, the highest detection rate at the individual-plot level was achieved by green shoulder VIs, such as GSIP₅₄₅ (0.48, norm-2), GSCR2_{MS} (0.43, norm-2), and GSCR1_{MS} (0.38, norm-3) (Figure 3). Red edge VIs performed slightly worse, with best results obtained with MR-DSWI1, MR-DSWI2, REIPLI, and NDRE (0.29-0.30, norm-2). Nevertheless, the detection rates decreased sharply at the multi-stand and multi-week scenarios. Considering the VIs previously mentioned, the best result for these scenarios was achieved by GSCR2_{MS} (0.23-0.25, norm-1). While RECP₆₈₅ and PRI_{550/530} also achieved similar detection rates for those scenarios, such results were not sustained in week 28 compared to other VIs. These results suggest that spectral changes in early stages of infestation were very subtle and could only be detected locally, i.e., by comparing infested trees with their neighbouring trees.

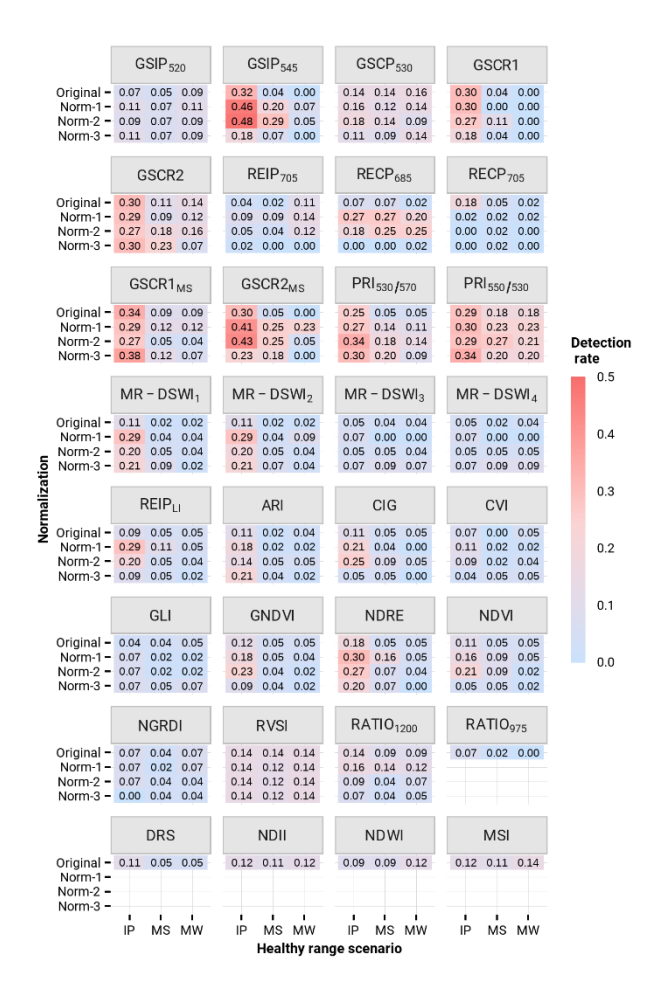


Figure 3. Detection rates of infested trees in week 26 (preemergence phase). Normalization: Original= original VI values, Norm= normalized VI values and respective baseline week. Healthy range scenario: IP= individual-plot, MS= multi-stand, MW= multi-week.

By week 28 when the offspring emergence began, detection improved for most VIs (Figure 4). Specifically, some green shoulder VIs reached detection of at least half of the infested trees across all three scenarios considered in this study, such as GSCR1_{MS} (0.68-0.52, norm-3) and GSCR2_{MS} (0.52-0.50, norm-1). GSCR1_{MS} with norm-3 showed the highest transferability, with only slight decreases in the detection rates comparing multistand (0.62) and multi-week (0.52) to individual-plot level detection (0.68). PRI_{530/570} had a similar detection rate at the individual-plot level, but transferability was lower, i.e., lower detection rates for multi-stand (0.39) and multi-week (0.34) scenarios. Red edge indices, on the other hand, did not perform well at the multi-week scenario. Their performance was limited to the individual-plot and multi-stand levels, with values close to 0.40 for MR-DSWI₁ and MR-DSWI₂ (0.38-0.43, norm-2). SWIR-based VIs consistently showed low detection rates, suggesting water content was not a primary indicator of bark beetle infestation in our study area.

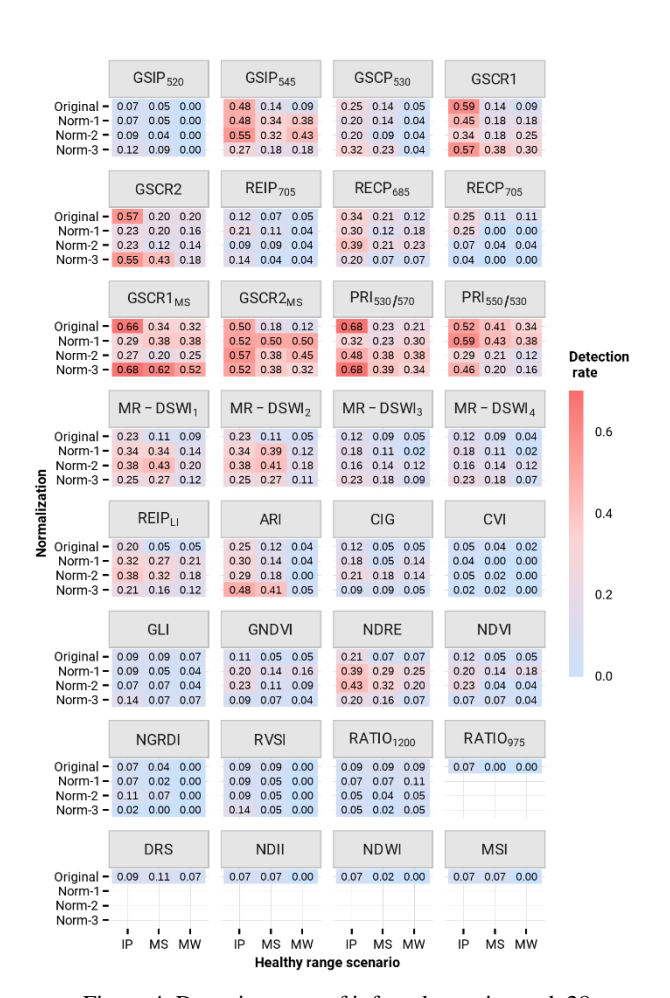


Figure 4. Detection rates of infested trees in week 28 (beginning of F1 filial generation emergence). Normalization: Original= original VI values, Norm= normalized VI values and respective baseline week. Healthy range scenario: IP= individual-plot, MS= multi-stand, MW= multi-week.

Figure 5 illustrates the challenge of detecting infested trees in week 26 considering the multi-stand scenario. We observed a clustering of VI values by field plot, but it was not clear whether this reflects differences in forest conditions, flight conditions (e.g., images captured on different days or times for different stands, illumination changes during the flight), or a combination of both. As a result, VI-based detection was limited at this stage, as most infested trees exhibited only minor deviations from healthy values, which were insufficient to surpass the broader detection thresholds used when considering healthy trees across multiple sites. In later weeks, however, infested trees showed larger deviations, enabling successful detection across all stands.

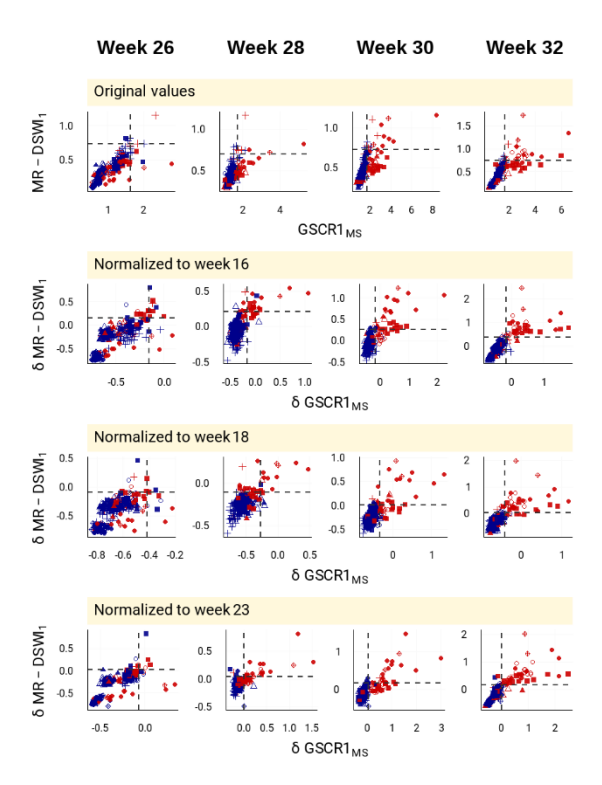


Figure 5. Values for GSCR1_{MS} and MR-DSWI₁ between weeks 26 and 32 for original values and values normalized to weeks 16, 18, or 23. Red markers represent infested trees and blue markers represent healthy trees. Different shapes represent different field plots. Dashed lines represent detection thresholds for each index considering the multi-stand scenario, i.e., all healthy trees from all field plots in a given week.

We observed that many VIs benefited from normalization, even though the optimal baseline week varied. Normalization to early-season values improved detection by reducing variability among healthy trees and enhancing the contrast between healthy and infested trees (Figure 6). While green shoulder indices had their performance enhanced with normalization, they also presented the best results using original VI values (e.g., GSCR1_{MS}, but also PRI_{550/530}). The same did not apply to red edge VIs, which heavily depended on normalization for detecting infested trees in our data. Therefore, green shoulder VIs can provide higher detection rates in single-image analysis, i.e., when a time series is not available.

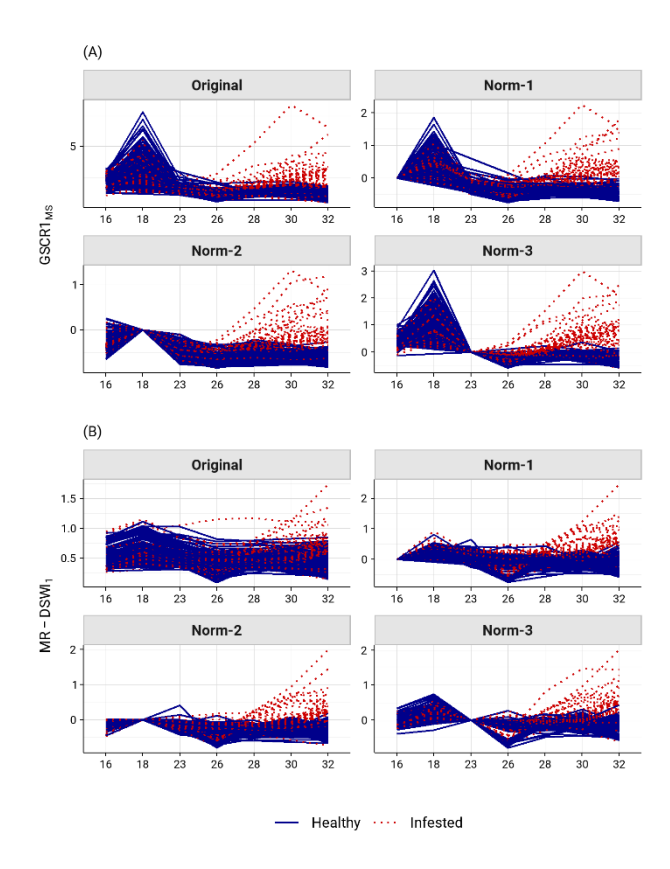


Figure 6. Evolution of GSCR1_{MS} (A) and MR-DSWI₁ (B) for healthy (in blue) and infested (in red) trees. Original= original VI values, Norm= normalized VI values and respective week.

4. Discussion

In our field survey, we recorded the first entrance holes in week 18, while most of the infested trees were first attacked from week 19 onwards. This indicates that data from week 26 reflects a situation of roughly 7-8 weeks after the bark beetle swarming. In Scandinavian forests, bark beetles typically emerge from the bark around 9-10 weeks after the adults bore into the bark, even though the specific timing depends on environmental conditions (Öhrn et al., 2014). Therefore, the low detection obtained in week 26 at the multi-stand scenario poses a challenge for effective preemergence detection, as infested trees cannot be easily separated from healthy trees across the landscape (Figure 5). Nevertheless, adopting the best VIs and best processing techniques (e.g., pixel selection and normalization) can be helpful to enable broad-scale monitoring, where spectral analysis can indicate specific sites where outbreaks are more likely to be happening to complement field efforts.

The fact that some green shoulder VIs presented consistent results at the multi-stand and multi-week scenarios suggests they are robust against a series of factors that can influence spectral signatures, such as forest properties (e.g., structural differences across trees and stands) and flight conditions (e.g., illumination, sun angles). Therefore, these VIs might be valuable metrics in monitoring forest disturbances from airborne platforms. These results reflect the high stability of green shoulder VIs observed for healthy trees between weeks 23 and 32 (Figure 6). We expect that this stability is not site-specific and persists for even longer, as Huo et al. (2024) also observed a similar trend in drone images collected between weeks 30 and 36 of 2021 in southern Finland.

Furthermore, these results indicate that green shoulder VIs have the highest potential to build models transferable to other time points and untrained areas. Generalizability has been a challenge for previous research using machine-learning models, leading to overfitting (Huo et al., 2023b). Nevertheless, a broader adoption of green shoulder VIs for forest disturbance monitoring is still limited by the spectral settings from sensors widely available (in particular commercial airborne sensors and spaceborne sensors with open data), which usually provide only one band in the green region around 550 nm, while calculating green shoulder VIs requires one additional band centred around 530 nm.

5. Conclusion

Green shoulder indices demonstrated the highest robustness and stability among all VIs for capturing stress-induced spectral changes across spatial and temporal scales. Their performance was further enhanced when normalized to early-season conditions, making these indices and techniques promising for detection of bark beetle infestations and other forest disturbances in southern Sweden.

Acknowledgements

This research was funded by the European Union with project RESDiNET [project grant 101078970 to LH], the Forest Damage Centre at the Swedish University of Agricultural Sciences [project grants 260FDC05, 260FDC57 and 260FDC44 to LH], the Swedish Research Council for Sustainable Development Formas [project grant 2024-00404 to LH]. We acknowledge Xiaoming Wang for the fieldwork conducted in 2023 and Aurora Bozzini for the assistance with the fieldwork in 2024, in addition to the fieldwork conducted by the authors.

References

Barnes, E., Clarke, T. R., Richards, S. E., Colaizzi, P., Haberland, J., Kostrzewski, M., Waller, P., Choi, C., Riley, E., & Thompson, T. L. (2000). Coincident detection of crop water stress, nitrogen status, and canopy density using ground based multispectral data. In *Proceedings of the fifth international conference on precision agriculture*, Bloomington, USA (Vol. 1619, No. 6).

Gitelson, A. A., Gritz †, Y., & Merzlyak, M. N. (2003). Relationships between leaf chlorophyll content and spectral reflectance and algorithms for non-destructive chlorophyll assessment in higher plant leaves. *Journal of Plant Physiology*, 160(3), 271–282. https://doi.org/10.1078/0176-1617-00887

Gitelson, A. A., Merzlyak, M. N., & Lichtenthaler, H. K. (1996). Detection of Red Edge Position and Chlorophyll Content by Reflectance Measurements Near 700 nm. *Journal of Plant Physiology*, 148(3), 501–508. https://doi.org/10.1016/S0176-1617(96)80285-9

Gitelson, A., Merzlyak, M., Zur, Y., Stark, R., & Gritz, U. (2001). Non-destructive and remote sensing techniques for estimation of vegetation status. Papers in Natural Resources, 273. In *Proceedings of the 3rd European Conference on Precision Agriculture*, Montpelier, France.

Green, P. J., & Silverman, B. W. (1993). Nonparametric Regression and Generalized Linear Models: A roughness penalty approach. Chapman and Hall/CRC. https://doi.org/10.1201/b15710

- Guyot, G., Baret, F., & Major, D. J. (1988). High spectral resolution: Determination of specral shifts between the red and the near infrared. *International Archives of Photogrammetry and Remote Sensing*, 11. https://www.indexdatabase.de/db/rsingle.php?id=23
- Hardisky, M. A., Klemas, V., & Smart, R. M. (1983). The Influence of Soil Salinity, Growth Form, and Leaf Moisture onthe Spectral Radiance of Spartina alterniflora Canopies. *Photogrammetry Engineering and Remote Sensing*, 49(1).
- Hunt, E. R., & Rock, B. N. (1989). Detection of changes in leaf water content using Near- and Middle-Infrared reflectances. *Remote Sensing of Environment*, 30(1), 43–54. https://doi.org/10.1016/0034-4257(89)90046-1
- Huo, L., Koivumäki, N., Oliveira, R. A., Hakala, T., Markelin, L., Näsi, R., Suomalainen, J., Polvivaara, A., Junttila, S., & Honkavaara, E. (2024). Bark beetle pre-emergence detection using multi-temporal hyperspectral drone images: Green shoulder indices can indicate subtle tree vitality decline. *ISPRS Journal of Photogrammetry and Remote Sensing*, 216, 200–216. https://doi.org/10.1016/j.isprsjprs.2024.07.027
- Huo, L., Koivumäki ,Niko, Näsi ,Roope, & Honkavaara, E. (2025). Sensitivity analysis of the Green Shoulder indices in preemergence detection of single trees attacked by European spruce bark beetle. *International Journal of Remote Sensing*, 46(9), 3513–3525. https://doi.org/10.1080/01431161.2025.2482747
- Huo, L., Lindberg, E., Bohlin, J., & Persson, H. J. (2023a). Assessing the detectability of European spruce bark beetle green attack in multispectral drone images with high spatial- and temporal resolutions. *Remote Sensing of Environment*, 287. Scopus. https://doi.org/10.1016/j.rse.2023.113484
- Huo, L., Persson, H. J., Bohlin, J., & Lindberg, E. (2023b). Green Attack or Overfitting? Comparing Machine-Learning- and Vegetation-Index-Based Methods to Early Detect European Spruce Bark Beetle Attacks Using Multispectral Drone Images. In *IGARSS 2023 2023 IEEE International Geoscience and Remote Sensing Symposium*, Pasadena, USA, pp. 546-549. https://doi.org/10.1109/IGARSS52108.2023.10282624
- Huo, L., Persson, H. J., & Lindberg, E. (2021). Early detection of forest stress from European spruce bark beetle attack, and a new vegetation index: Normalized distance red & SWIR (NDRS). Remote Sensing of Environment, 255, 112240. https://doi.org/10.1016/j.rse.2020.112240
- Jackson, T. J., Chen, D., Cosh, M., Li, F., Anderson, M., Walthall, C., Doriaswamy, P., & Hunt, E. R. (2004). Vegetation water content mapping using Landsat data derived normalized difference water index for corn and soybeans. *Remote Sensing of Environment*, 92(4), 475–482. https://doi.org/10.1016/j.rse.2003.10.021
- Kärvemo, S., Huo, L., Öhrn, P., Lindberg, E., & Persson, H. J. (2023). Different triggers, different stories: Bark-beetle infestation patterns after storm and drought-induced outbreaks. *Forest Ecology and Management*, 545, 121255. https://doi.org/10.1016/j.foreco.2023.121255
- Kautz, M., Feurer, J., & Adler, P. (2024). Early detection of bark beetle (*Ips typographus*) infestations by remote sensing A critical review of recent research. *Forest Ecology and*

- *Management*, 556, 121595. https://doi.org/10.1016/j.foreco.2023.121595
- Li, N., Huo, L., & Zhang, X. (2024). Using only the red-edge bands is sufficient to detect tree stress: A case study on the early detection of PWD using hyperspectral drone images. *Computers and Electronics in Agriculture*, 217, 108665. https://doi.org/10.1016/j.compag.2024.108665
- Luo, Y., Huang, H., & Roques, A. (2023). Early Monitoring of Forest Wood-Boring Pests with Remote Sensing. *Annual Review of Entomology*, 68, 277–298. https://doi.org/10.1146/annurevento-120220-125410
- Merton, R. N. (1998). Monitoring community hysteresis using spectral shift analysis and the red-edge vegetation stress index. In *Proceedings of the Seventh Annual JPL Airborne Earth Science Workshop*, Pasadena, USA.
- Öhrn, P., Långström, B., Lindelöw, Å., & Björklund, N. (2014). Seasonal flight patterns of *Ips typographus* in southern Sweden and thermal sums required for emergence. *Agricultural and Forest Entomology*, 16(2), 147–157. https://doi.org/10.1111/afe.12044
- Peñuelas, J., Gamon, J. A., Fredeen, A. L., Merino, J., & Field, C. B. (1994). Reflectance indices associated with physiological changes in nitrogen- and water-limited sunflower leaves. *Remote Sensing of Environment*, 48(2), 135–146. https://doi.org/10.1016/0034-4257(94)90136-8
- Pu, R., Foschi ,L., & Gong, P. (2004). Spectral feature analysis for assessment of water status and health level in coast live oak (*Quercus agrifolia*) leaves. *International Journal of Remote Sensing*, 25(20), 4267–4286. https://doi.org/10.1080/01431160410001705114
- Rouse, J. W., Haas, R. H., Schell, J. A., & Deering, D. W. (1973). Monitoring vegetation systems in the Great Plains with ERTS.
- Tucker, C. J. (1979). Red and photographic infrared linear combinations for monitoring vegetation. *Remote Sensing of Environment*, 8(2), 127–150. https://doi.org/10.1016/0034-4257(79)90013-0
- Vincini, M., Frazzi, E., & D'Alessio, P. (2008). A broad-band leaf chlorophyll vegetation index at the canopy scale. *Precision Agriculture*, 9(5), 303–319. https://doi.org/10.1007/s11119-008-9075-z